

# Connecting processing-capable quantum memories over telecommunication links via quantum frequency conversion

M S Shahriar<sup>1,2</sup>, P Kumar<sup>1,2</sup> and P R Hemmer<sup>3</sup>

<sup>1</sup> Department of EECS, Northwestern University, 2145 Sheridan Road, Evanston, IL 60208, USA

<sup>2</sup> Department of Physics and Astronomy, Northwestern University, 2145 Sheridan Road, Evanston, IL 60208, USA

<sup>3</sup> Department of EECS, Texas A&M University, 3128 TAMU, College Station, TX 77843, USA

E-mail: [prhemmer@ece.tamu.edu](mailto:prhemmer@ece.tamu.edu)

Received 5 January 2012, in final form 24 February 2012

Published DD MM 2012

Online at [stacks.iop.org/JPhysB/45/000000](http://stacks.iop.org/JPhysB/45/000000)

## Abstract

For quantum information processing (QIP), it is important to have a long-lived quantum memory (QM), coupled to other QMs and quantum processors (QP). However, QM and QP systems demonstrated so far suffer from many limitations, and in the near future a single platform will not have the optimal version of all the components needed for QIP. Thus, it is also important to be able to couple quantum bits in different systems, for example, Rb atoms and NV diamond, preferably using telecom fibres. In this paper, we describe a quantum frequency converter (QFC) that will perform this telecom band qubit conversion. The QFC is based on periodically poled lithium niobate waveguides. For concreteness, we consider specific examples: the conversion of a 780 nm or 795 nm Rb qubit to the telecom band and the conversion of a 637 nm photonic NV diamond qubit to the telecom band, as well as the inverse processes. We show that interface fidelity exceeding 95% should be feasible. Given the storage times  $\sim 1$  s already demonstrated in the solid-state systems, and the recent demonstrations of spin-photon entanglement with the NV and entanglement of the NV spin with a superconducting flux qubit operating in the microwave region near 2.88 GHz, such a link would provide the key interface needed to build a quantum internet.

**Q1** (Some figures may appear in colour only in the online journal)

## 1. Introduction

In any quantum information system, such as those used for secure communication and computation, one needs the ability to send quantum information between the nodes of the system and to store this information in a manner that retains the necessary quantum correlations. Quantum memories also play an important role in entanglement purification protocols. For example, a modified form of the Duan–Lukin–Cirac–Zoller protocol [1] uses atomic memories by collecting one photon of an entangled pair after its twin has been detected [2]. This system thus allows for the long-haul quantum key distribution. The optimum strategy for transmitting and storing quantum information can be quite different for different subsystems even within a given system. For example, entanglement

involving orbital angular momentum states [3, 4], such as Laguerre–Gauss states, is a preferred way of transmitting quantum information over a free-space link, whereas time-energy entanglement [5] is preferred for transmitting quantum information over a fibre-optic link or within a guided-wave geometry. Also, even within the context of quantum memories, different strategies may be optimal for the construction of a short-term quantum memory (such as a buffer) versus a long-term memory. Thus, there is a need to develop complementary strategies for the transmission and storage of quantum information. There is also a need to develop means for converting quantum resources, such as entanglement, from one physical degree of freedom to another within a quantum network.

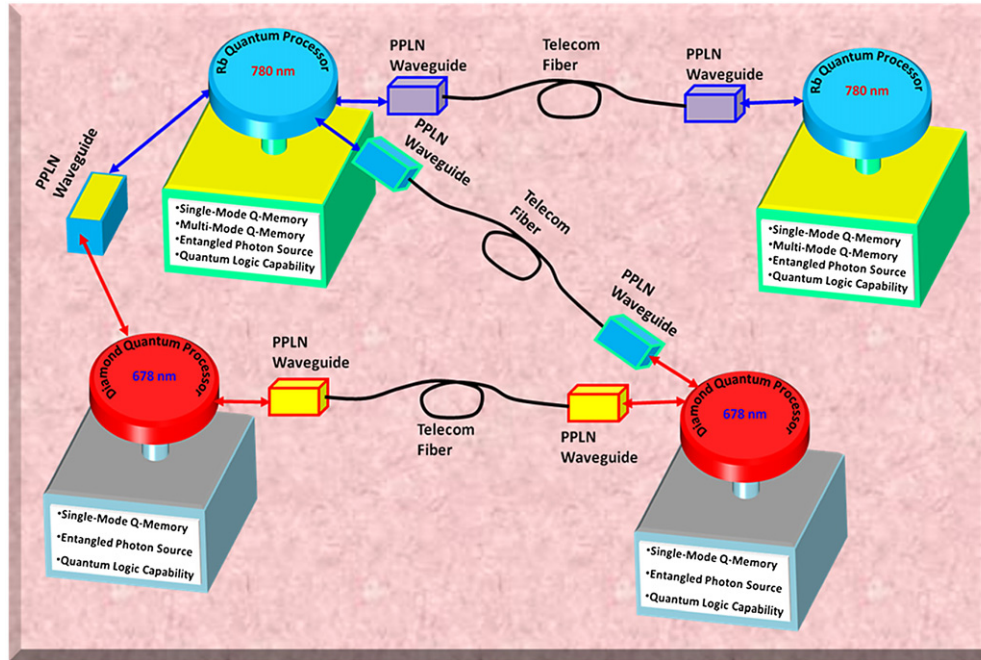


**Figure 1.** Schematic illustration of telecommunication band links between quantum memories of different types.

In this paper, we describe possible techniques for connecting different types of quantum memories over telecommunication band (TB) links, using quantum frequency converters (QFCs) [6] based on periodically poled lithium niobate (PPLN) waveguides. The quantum memory linking system is illustrated schematically in figure 1. Briefly, we consider two types of quantum memories: one using  $^{87}\text{Rb}$  atoms and the other using nano-structures of diamond containing single nitrogen-vacancy colour centres (NVCC). The Rb quantum memory, augmented for processing capabilities, is assumed to have the following capabilities: single-mode quantum memory, multi-mode quantum memory, conversion of atomic qubits to photonic qubits (PQs) at 780 nm, deterministic quantum logic operations among memory elements, production of entangled photons and measurement of Bell states. The diamond quantum memory, also augmented for processing capabilities, is assumed to have the following capabilities: single-mode quantum memory, production of entangled photons and measurement of Bell states. A processing-capable quantum memory, which can also be called an active quantum memory, is defined as a QM that can couple to another QM via quantum logic. Note that for NVCC the recently demonstrated entanglement of photons with spin [7] as well as entanglement of spin with superconducting flux qubits [8] may allow extending this network to include superconducting qubits operating near the 2.88 GHz NV spin transition frequency. A more detailed discussion of the different types of qubits available appears in [9, 10].

Using the technique of difference frequency generation in a PPLN waveguide, we consider here the prospect of developing three different types of QFCs: (a) converting 637 nm (diamond) photonic qubit to TB, (b) converting 780 or 795 nm (Rb) photonic qubit to TB and then to 637 nm,

and (c) converting 637 nm PQ to a 780 nm PQ. Consider, for example, the parameters involved in realizing the QFC in item (a) above. A PPLN waveguide pumped with a YAG laser at 1064 nm can be quasi phase matched for the process of generating the difference frequency between 637 and 1064 nm, corresponding to 1593.5 nm. For a 2 cm long and 5  $\mu\text{m}$  mode-diameter waveguide, and with a quasi CW pump for a photon of 100 ns duration, the average power will be only 10 mW. For cases (b) and (c), the parameters needed are similarly accessible.

The rest of the paper is organized as follows. In section 2, we describe the architectures of using PPLN-based waveguides for linking different types of quantum memories. In section 3, we describe a quantum memory based on ensembles of Rb atoms, augmented for processing capabilities. In section 4, we describe an NV-diamond-based quantum memory, also augmented for processing capabilities. In section 5, we present the summary and the outlook.

## 2. Quantum frequency converters

Quantum frequency conversion (QFC) is a process in which an input light beam is converted into an output beam of different optical frequency while preserving its quantum state [11]. It plays an important, twofold role in the proposed quantum-memory network. In the first place, it serves as the interface between memory devices in different material form where photonic qubits of different wavelengths are involved. Secondly, it enables quantum telecommunication between distant memory devices using the existing fibre-based, low-loss telecommunication infrastructure. Here, we describe a complete set of QFC devices that are suitable for the interface between the Rb-ensemble and NV-diamond-based memory devices, as well as the fibre-based quantum telecommunication among them.

The proposed QFC devices are based on the second-order nonlinear process in  $\chi^{(2)}$  media. To see how this comes about, let us consider the coupling of three z-propagating optical waves of angular frequencies  $\omega_j$  satisfying  $\omega_3 = \omega_1 + \omega_2$ . The coupling is described by the following general coupled equations [12]:

$$\begin{aligned} \frac{dE_3}{dz} &= i \frac{\omega_3 K}{n_3 c} E_1 E_2 e^{i\Delta k z}, & \frac{dE_1}{dz} &= i \frac{\omega_1 K}{n_1 c} E_3 E_2^* e^{-i\Delta k z}, \\ \frac{dE_2}{dz} &= i \frac{\omega_2 K}{n_2 c} E_3 E_1^* e^{-i\Delta k z}, & \Delta k &= k_1 + k_2 - k_3, \end{aligned} \quad (1)$$

where  $k_j = n_j \omega_j / c$  is the wave-vector magnitude for each wave  $E_j$  and  $K$  is the effective nonlinear coupling coefficient in the waveguide— $d_{33}$ , for example, in the z-cut periodically poled lithium niobate (PPLN) waveguide. The above coupled equations can be solved exactly for the arbitrary phase-mismatch  $\Delta k$  in terms of hyper-geometric functions. For the QFC purpose, however, we consider only the phase-matching case with  $\Delta k = 0$ .

There are three cases of interest to us. The first case is of second-harmonic generation (SHG), in which the fundamental field ( $E_1 = E_2 = E_\omega$ ) is monotonically converted into a frequency-doubled field  $E_3 = E_{2\omega}$ . The second case of interest is of sum-frequency generation (SFG) wherein one of the lower-frequency fields is allowed to deplete, say the  $E_1$  field at  $\omega_1$ , whereas the other lower-frequency field  $E_2$  remains strong and undepleted. (Usually, the depleted and undepleted fields are referred to as the signal and the pump, respectively.) In this case, the power of the signal field is periodically exchanged between the  $\omega_1$  field  $E_1$  and the sum-frequency field  $E_3$ . The period of power exchange is dependent on the intensity of the pump field at  $E_2$  and hence is optically controllable. Full exchange of power between  $E_1$  and  $E_3$  can occur under the condition of phase-matching, i.e.  $\Delta k = 0$ , for which one obtains

$$E_3(z) = E_3(0) \cos \kappa z + i e^{i\phi_2} (n_1 \omega_3 / n_3 \omega_1)^{1/2} E_1(0) \sin \kappa z, \quad (2)$$

where  $\phi_2$  is the phase of the pump field  $E_2$  and  $\kappa = (\omega_1 \omega_3 K^2 / n_1 n_3 c^2)^{1/2} E_2$  is the SFG coefficient proportional to the square root of pump power. A similar equation for  $E_1(z)$  is obtained by interchanging 1 and 3. The third case of interest is the difference frequency generation (DFG) process, which is similar to SFG but with a higher frequency field depleted to create a lower frequency field. For both DFG and SFG, by choosing  $\kappa z = (j+1/2)\pi$  where  $j$  is an integer, the power exchange is (ideally) 100%, whereby the input signal converts completely into an output light of different frequency.

The above analysis is classical. In the quantum domain, the equation of motion for optical fields can be obtained by the routine second-quantization method. Consider, for example, the case of SFG. For a strong coherent pump and a weak propagation loss of light travelling through the waveguide, the annihilation operators of input ( $\hat{a}_1, \hat{a}_3$ ) and output ( $\hat{b}_1, \hat{b}_3$ ) signal fields obey [13]

$$\hat{b}_1 = \hat{a}_1 \cos \kappa z - \hat{a}_3 \sin \kappa z, \quad \hat{b}_3 = \hat{a}_3 \cos \kappa z + \hat{a}_1 \sin \kappa z. \quad (3)$$

Choosing the pump intensity such that  $\kappa z = \pi/2$ , the above equations become

$$\hat{b}_1 = -\hat{a}_3, \quad \hat{b}_3 = \hat{a}_1. \quad (4)$$

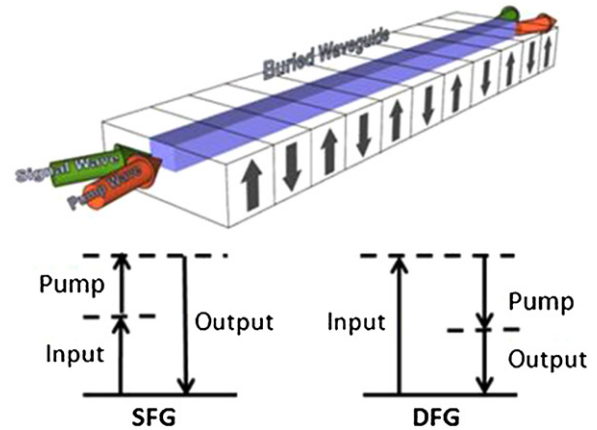


**Figure 2.** The QFC schematic. Upper: the buried PPLN waveguide; lower left and right: the relevant SFG and DFG processes, respectively.

This result shows that with appropriate pump intensity and waveguide length, the input signal can be completely converted into an output of a different frequency while its quantum state is preserved. It is this state-preserving feature of SFG and DFG that enables the QFC operation.

To build QFC devices compatible with the quantum-memory devices described in sections 3 and 4, we consider the use of planar PPLN waveguides as the second-order nonlinearity media. The use of such waveguides has several advantages. First of all, they are commercially available with well-developed fabrication technology. Second, the lithium niobate material has a large nonlinear coefficient ( $>20 \text{ pm V}^{-1}$ ) for efficient QFC and a wide transparent widow ( $\sim 350\text{--}5200 \text{ nm}$ ) that allows applications over a broad wavelength band. Third, the quasi-phase matching (QPM) technique, in which periodic domain inversion is used to compensate for the material phase mismatching ( $\Delta k \neq 0$ ), has been well established for both SFG and DFG over a wide range of wavelengths. Lastly, the background scattering in the lithium niobate material is weak, resulting in a rather low quantum noise and thus high purity of the frequency-converted photons. We consider using double-layer (‘buried’) PPLN waveguides, whose schematic is shown in figure 2. For fabrication, such waveguides are produced by first applying proton exchange (PE) to a bulk PPLN substrate to create a layer strip of  $\text{HNbO}_3$ . (Alternatively, one can apply PE during the growth stage of PPLN.) Then, a reverse PE process is applied to create a second layer of  $\text{LiNbO}_3$  on top of the  $\text{HNbO}_3$  layer. For this structure, only extraordinary light can be guided. Compared to in-diffusion or PE PPLN waveguides, the buried PPLN waveguides have the advantage of stronger second-order nonlinearity and a weaker waveguide loss. Also in figure 2, we show the SFG and DFG level schemes that can be employed to perform QFC.

Using the buried PPLN waveguides as basic elements, we now describe the process for constructing the quantum-state-preserving QFC circuits. First of all, to preserve the time-energy states of photons, one needs to use a pump beam that is flat over the entire time interval containing the temporal Hilbert space of the signal photons. Then, to preserve the polarization

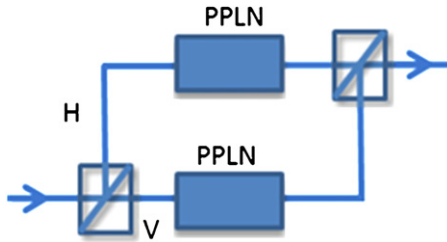


**Figure 3.** Polarization-preserving QFC element. See the text for details.

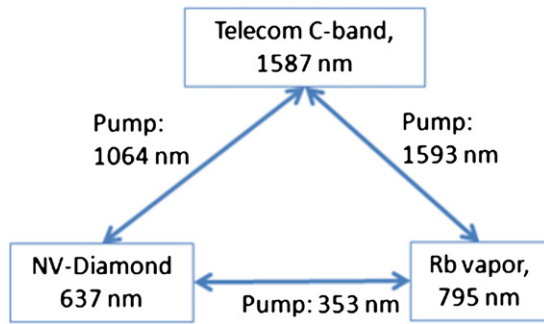


**Figure 4.** The QFC scheme for use with Rb D1-line transition.

states, one would use a two-PPLN setup, as shown in figure 3. It consists of a polarized beamsplitter (PBS) to separate the H and V polarization components of input photons. The H and V components then each undergo two separate QFC processes in two independent PPLN waveguides. The two waveguides are identical but with the optical axis of the waveguide rotated by  $90^\circ$  relative to each other. The two polarization components are then recombined at the second PBS to produce a frequency-converted output whose polarization state is preserved.

Using the above QFC circuit, it is possible to develop systematical QFC schemes for use with the atomic-ensemble and NV-centre-based QM devices. As both the Rb  $D_1$ -line (795 nm) and  $D_2$ -line (780 nm) transitions can be used for ensemble-based QMs, we describe two QFC schemes that are compatible with the two transitions. The first QFC scheme is shown in figure 4, wherein three wavelengths of interests are involved. They are 637 nm associated with NV-diamonds, 795 nm with the Rb  $D_1$  line and 1587 nm in the telecom L-band for use in quantum telecommunication via low-loss optical fibres. For the QFC between 637 and 1587 nm, one would use a Nd:YAG laser at 1064 nm as the pump. The PPLN waveguide is designed to be QPM for the  $1587\text{ nm} + 1064\text{ nm} \downarrow 637\text{ nm}$  process. For the QFC between 795 and 1587 nm, one would use a 1593 nm pump with the waveguide QPM for the  $1587\text{ nm} + 1593\text{ nm} \downarrow 795\text{ nm}$  process. Finally, for the direct QFC between 795 and 637 nm, a pump at 353 nm is used, and the waveguide is periodically poled to be QPM for the  $795\text{ nm} + 637\text{ nm} \downarrow 353\text{ nm}$  process. Here, in order to obtain the 353 nm pump, a 1059 nm fibre laser could be used as the source. The 1059 nm laser is first frequency doubled to create a 529.5 nm light using a PPLN that is QPM for the SHG for this wavelength. The 529.5 nm light is then combined with the 1059 nm laser to create the desired 353 nm pump via SFG. In practice, the two processes of SHG and

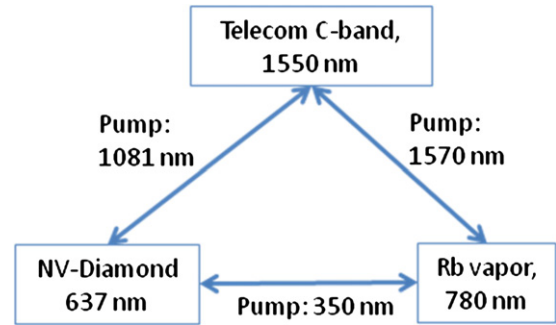


**Figure 5.** The QFC scheme for use with Rb  $D_2$ -line transition.

SFG can be implemented in a single PPLN waveguide with two poling periods.

Similarly, the second QFC scheme deals with 637 nm photons associated with NV-diamonds, 780 nm photons with the Rb  $D_2$ -line transition and 1550 nm photons in the telecom C-band, as shown in figure 5. To drive the QFC between 637 and 1550 nm, one would use a 1081 nm pump and a waveguide that is QPM for the  $1550\text{ nm} + 1081\text{ nm} \downarrow 637\text{ nm}$  process. For QFC between 780 and 1550 nm, one would use a 1570 nm pump with a waveguide QPM for the  $1550\text{ nm} + 1570\text{ nm} \downarrow 780\text{ nm}$  process. Finally, to implement QFC for the 637 and 780 nm light, one would use a pump at 350 nm and a waveguide QPM for the  $637\text{ nm} + 780\text{ nm} \downarrow 350\text{ nm}$  process. Again, the 350 nm laser can be produced adopting successive SHG and SFG processes using a 1050 nm laser from a Ytterbium fibre amplifier.

### 3. Rubidium quantum memory

A neutral alkali atom held in a far-off-resonant trap (FORT) represents a potentially ideal quantum system which can serve as a processing-capable QM, when coupled strongly to a cavity photon. However, such a system requires the use of a high finesse cavity with a microscopic volume. This geometry severely constrains the usage of such a system. An alternative approach makes use of an ensemble of atoms as the quantum system. Such an ensemble can serve as a QM, and can be used to produce entangled states of photons. It can also be used to entangle two QMs separated spatially. However, this process is probabilistic, which vastly limits the utility of such a protocol. While ‘the single atom in a cavity’ and ‘an ensemble in free space’ appear to be two distinctly different systems, we have recently shown [14, 15] that these two processes merely represent two extremes of a generalized technique:  $M$  atoms in a cavity with finesse  $N$ . The first case represents one extreme, where  $M = 1$  and  $N$  is a large number. The second case represents the other extreme, where  $M$  is a large number and  $N = 1$ . Specifically, we have shown how the general system with  $M > 1$  and  $N > 1$  can be used to realize a deterministic quantum bit, via the process of light shift blockade (LSB) that occurs naturally<sup>14,15</sup>. In particular, if one uses a modest number of atoms (e.g.,  $M \sim 10^5$ ) with a relatively low finesse cavity ( $N \sim 10^2$ ), the resulting system allows one to get around the limitations of both extremes.

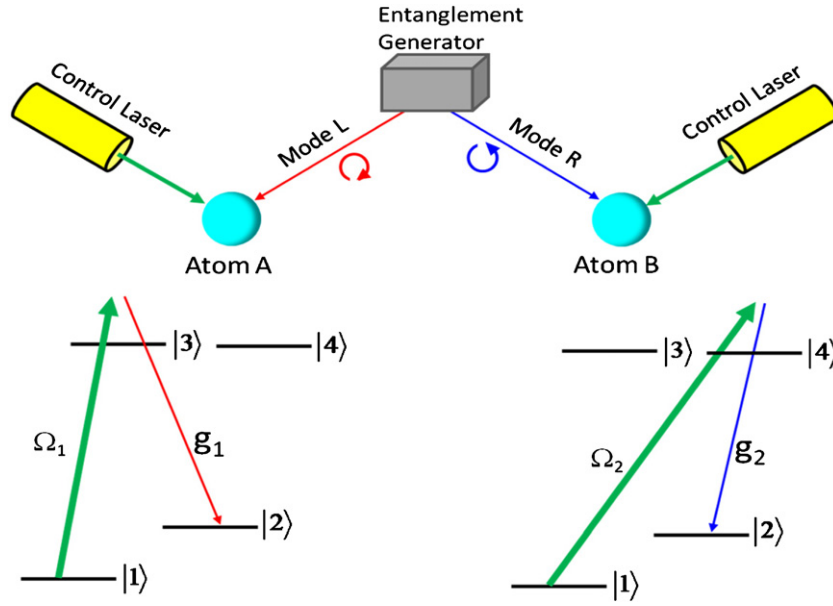


**Figure 6.** Schematic illustration of storage of an atomic quantum memory.

Q2

Experimentally, an array of such ensembles could be realized by using an array of FORT potentials, loaded from a magneto-optic trap (MOT), enclosed inside a relatively large MEMS-based cavity. Using two such apparatuses, it would be possible to demonstrate<sup>14</sup>: (1) loading of an arbitrary PQ into an atomic ensemble QM, with a storage time of more than 1 s, and a fidelity >90%; (2) generation of entanglement between two QMs within the same apparatus; (3) generation of entanglement between two remote QMs, in a deterministic manner, using the Pellizari–Gardiner–Cirac–Zoller protocol [16]; and (4) measurement of all four Bell states, using the Lloyd–Shahriar–Hemmer–Shapiro protocol [17]. These capabilities, in turn, imply that the system could be used for realizing essentially any protocol in QIP, including entanglement swapping quantum teleportation and entanglement purification [18].

The basic concept for an atomic quantum memory is illustrated in figure 6. Consider an unspecified source that produces a pair of entangled photons, in two spatial modes: L and R. In general, such a state can be written as  $\alpha|0\rangle_L|0\rangle_R + \beta|0\rangle_L|1\rangle_R + \gamma|1\rangle_L|0\rangle_R + \xi|1\rangle_L|1\rangle_R$ . For example,  $\alpha = 0$ ,  $\xi = 0$  and  $\beta = -\gamma = 1/\sqrt{2}$  would represent a maximally entangled state. Each mode is now made to interact with a distinct atom. Prior to the interaction, the quantum state of the two atoms is unentangled and expressed simply as  $|1\rangle_A|1\rangle_B$ . For the particular example of parameters, the joint state of the photons and atoms is thus given by  $(1/\sqrt{2})(|0\rangle_L|1\rangle_R - |1\rangle_L|0\rangle_R)|1\rangle_A|1\rangle_B$ . We assume that the L mode is coupled to the 1–3 transition and the R mode is coupled to the 1–4 transition. By applying a properly timed pair of pulses (with the Rabi frequencies  $\Omega_1$  and  $\Omega_2$ ) from the two control laser beams, an optically off-resonant but two-photon resonant Raman transition is carried out in each atom. Here, the Rabi frequencies due to the L and R photons are  $g_1$  and  $g_2$ , respectively. The strength of a given  $g$  is determined by three factors: the dipole

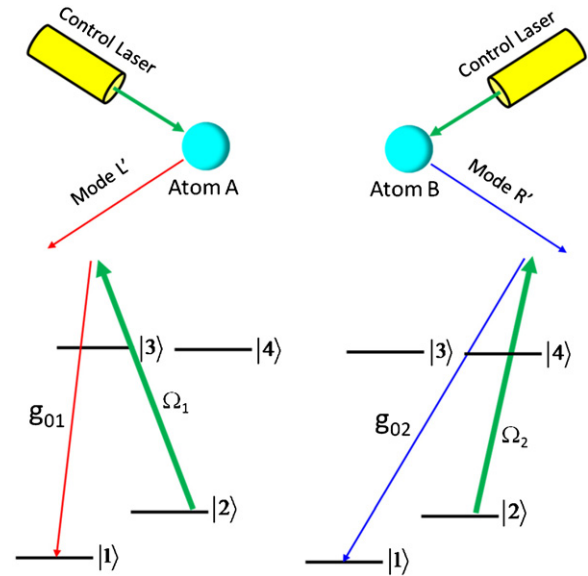


**Figure 7.** Schematic illustration of readout from an atomic quantum memory.

moment of the transition, the energy of a single photon and the mode volume of the photon. For a free space photon, the effective mode volume is determined by the transverse spatial profile and the finite temporal duration. After the Raman interactions, the quantum state of the combined system becomes  $(1/\sqrt{2})|0\rangle_L|0\rangle_R(|1\rangle_A|2\rangle_B - |2\rangle_A|1\rangle_B)$ , producing a maximally entangled state between the atoms.

The process for transferring the quantum information from the pair of atoms to a pair of photons is illustrated schematically in figure 7. For atom A, the readout laser pulse is now applied on the 2–3 transition. If the atom were in state 2, this will produce an anti-Stokes photon, corresponding to the 1–3 transition, and detuned to match the two-photon resonance condition, designated again as the L'-mode. Here,

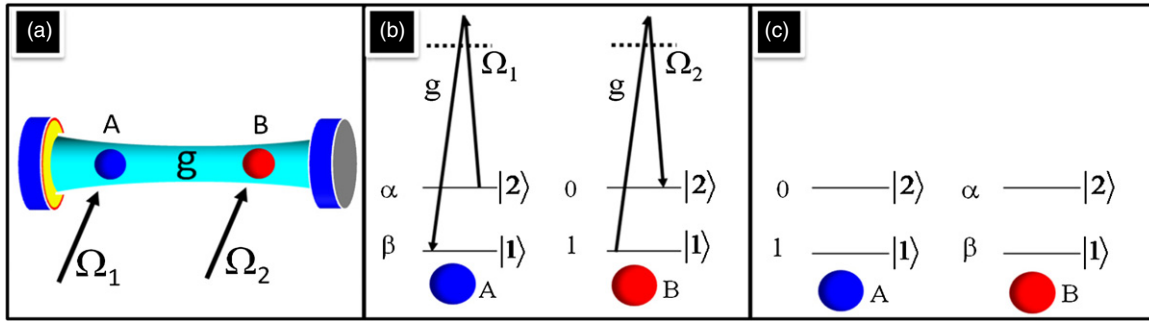


Figure 8. Illustration of quantum state transfer between atoms in a cavity.

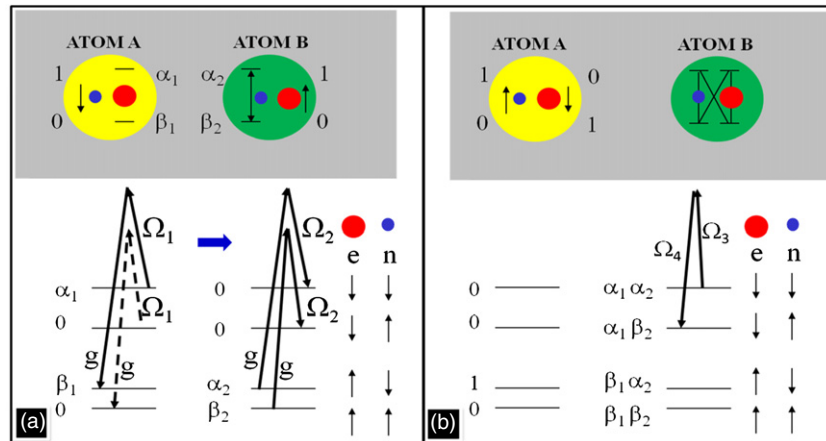


Figure 9. Illustration of loading two qubits into a single atom, for a CNOT gate operation between the atoms.

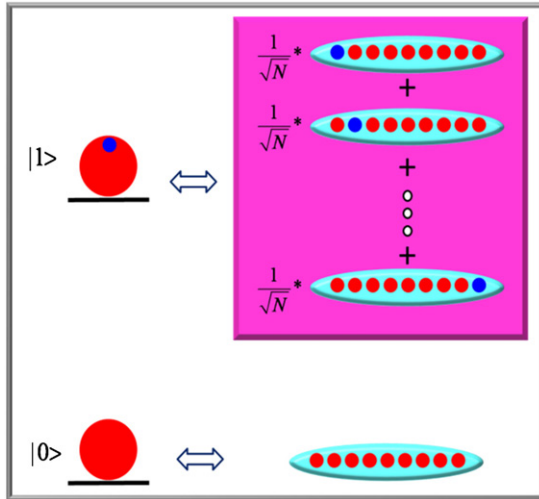
the Rabi frequency for the single photon will correspond to the mode that is most efficiently matched to the readout pulse. If the atom were in state 1, no photon would be produced. A similar process is carried out in atom B, and the net result after the readout process is a quantum state given by  $(1/\sqrt{2})(|0\rangle_L|1\rangle_R - |1\rangle_L|0\rangle_R)|1\rangle_A|1\rangle_B$ .

Such a passive quantum memory (PQM) is adequate for situations where the primary objective is to convert a flying qubit to a stationary qubit, serving as a buffer, in order to extend the useful lifetime of the quantum information. However, a more useful quantum memory would be a system that can perform arbitrary quantum gate operations: an active quantum memory (AQM). In principle, the single-atom PQM system described above can be modified to act as an AQM by making use of a cavity to couple the atoms. The basic process behind such a coupling is illustrated in figure 8. Consider two atoms inside a cavity, with atom B in the ground state and atom A in a quantum superposition (figure 8(a)). A laser pulse applied to atom A transfers the quantum state to the cavity, in a superposition of zero photon and one photon (figure 8(b)). Another laser pulse applied to atom B then transfers this quantum state to atom B (figures 8(b) and (c)). Here, the Rabi frequency corresponding to a single photon is determined by the cavity mode volume.

A generalization of this basic concept can be used to realize a controlled-NOT (CNOT) between the two atoms, as illustrated in figure 9. Here, each atom is assumed to have four metastable ground states, which can be modelled effectively as the space spanned by the spin-up and spin-down states of an

electron and the nucleus, for example. At the onset, the qubit in atom A is encoded in the nucleus (blue circle), while the qubit in atom B is encoded in the electron (red circle). A laser field applied to atom A converts the electronic quantum state to the cavity. Another laser field applied to atom B transfers this quantum state to the electron in atom B (figure 9(a)). The net result is that the both bits of quantum information, unentangled, are now inside atom B (figure 9(b)). An internal transition between two of the four states, realized by another Raman transition using two laser beams, entangles the electron and the nucleus inside atom B. For example, a transition between the top two states (figure 9(b)) would correspond to a CNOT operation where the electron nuclear spin is flipped if and only if the electron spin is down. The reverse of the process shown in figure 9(a) transfers the electronic quantum state from atom B to atom A. The end result is that atoms A and B are now entangled, having undergone a CNOT operation. It is well known that a CNOT is a universal quantum gate, so that the ability to carry out this operation is tantamount to the ability to perform any quantum logic operation.

The process for storing and retrieving an entangled photon pair, as illustrated in figures 6 and 7, is impractical because the vacuum Rabi frequencies achievable in free space are too weak. However, this scheme can easily be modified to a pair of atoms held in a cavity, with the richer set of energy levels, as shown in figures 8 and 9. In this case, the photon modes would be coupled into the cavity prior to storage. Similarly, the retrieved information will be encoded in the cavity mode first, and can then be released into a free space mode, or into



**Q3** Figure 10. Illustration of collective excitation in an ensemble.

an optical fibre, for long distance propagation. Furthermore, as shown in [17], it is possible to perform measurements of all four Bell states in such a system as well. Thus, two atoms held inside a cavity form the type of AQM that would satisfy virtually all requirements of quantum information processing (QIP).

There are several technological challenges in realizing such a system. The most significant of these challenges is the fact that the vacuum Rabi frequency for a single atom, even inside a cavity, is rather weak. To make this strong enough, it is necessary to employ a very small cavity, with a very high finesse. The geometry of such a cavity makes it difficult to trap a set of single atoms and to perform the necessary control operations.

This problem can be circumvented by using an ensemble of atoms as an individual quantum system. The basic concept behind this approach is illustrated in figure 9, where each atom

is assumed to be a two-level system. The ground state of the ensemble corresponds to each of the  $N$  atoms being in the ground state. The first excited state is a coherent superposition of  $N$  states, each of which has only one of the atoms in the excited state. For a single photon interacting identically with each atom, the ensemble also behaves as a two-level system, with the property that the coupling rate is now enhanced by  $\sqrt{N}$ .

In order to realize a simple quantum memory, it is necessary to consider a situation where each atom has three energy levels: two metastable levels and one high-energy state coupled optically, forming a  $\Lambda$  system. A typical excitation with such an ensemble would use an optical field on each leg. Under such an excitation, the ensemble no longer behaves as a three-level ( $\Lambda$ ) system. Instead, we get a cascade of states, corresponding to absorptions of the  $n$  photons from each mode, where  $n$  can range from 1 to a very large integer. This is illustrated in figure 11, with the collective states defined in figure 12. The cascade corresponding to the optical transitions alone can be ignored under most circumstances, because of detuning. However, the cascades corresponding to the Raman transitions must be taken into account.

In the case where mode 2 corresponds to a quantum state with zero or one photon, the Raman process is terminated within a single- $\Lambda$  system, as indicated by the shaded region. This is the case corresponding to the storage and recall of single-photon quantum states, akin to what is shown in figures 6 and 7. Thus, it is possible to use an ensemble to realize a robust PQM; several groups have demonstrated such a memory already.

Consider next the prospect of using such an ensemble to perform quantum gate operations, of the type illustrated in figure 9. For the CNOT gate operation, it is necessary to use a Raman transition where both legs are excited by coherent states with a large mean number of photons. Similar operations are also necessary for quantum rotations within a single qubit, as

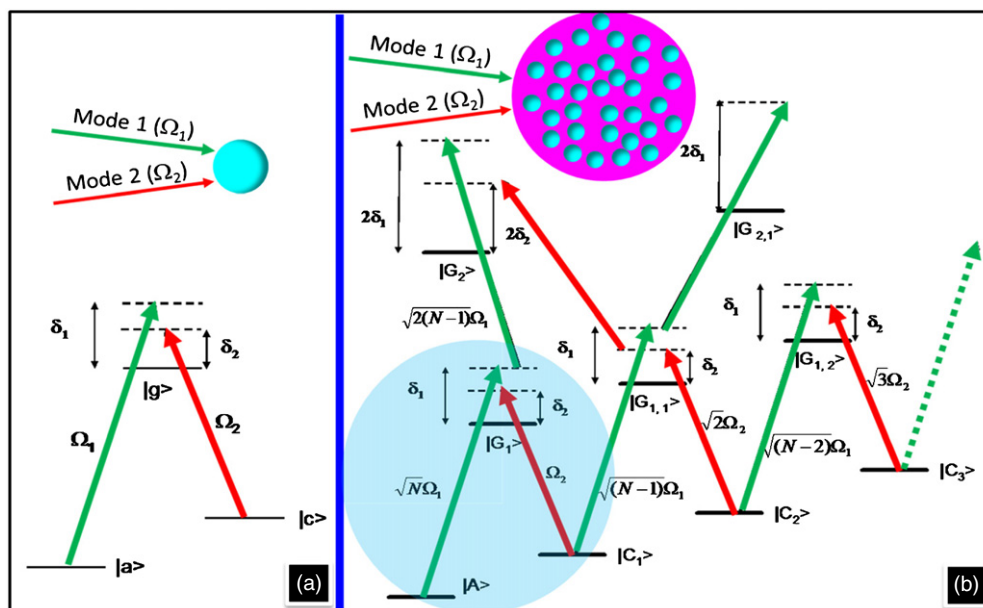


Figure 11. Illustration of cascades of transitions in an ensemble.

$$\begin{aligned}
 |A\rangle &\equiv |a_1, a_2, \dots, a_N\rangle; \quad |G_1\rangle \equiv \frac{1}{\sqrt{N}} \sum_{j=1}^N |a_1, a_2, \dots, g_j, \dots, a_N\rangle \\
 |C_1\rangle &\equiv \frac{1}{\sqrt{N}} \sum_{j=1}^N |a_1, a_2, \dots, c_j, \dots, a_N\rangle \\
 |G_2\rangle &\equiv \frac{1}{\sqrt{N C_2}} \sum_{j,k(j \neq k)}^{N C_2} |a_1, a_2, \dots, g_j, \dots, g_k, \dots, a_N\rangle \\
 |C_2\rangle &\equiv \frac{1}{\sqrt{N C_2}} \sum_{j,k(j \neq k)}^{N C_2} |a_1, a_2, \dots, c_j, \dots, c_k, \dots, a_N\rangle \\
 |G_{1,1}\rangle &\equiv \frac{1}{\sqrt{2^N C_2}} \sum_{j,k(j \neq k)}^{2^N C_2} |a_1, a_2, \dots, g_j, \dots, c_k, \dots, a_N\rangle \\
 |G_{2,1}\rangle &\equiv \frac{1}{\sqrt{Z}} \sum_{(j \neq k \neq l)}^Z |a_1, a_2, \dots, g_j, \dots, g_k, \dots, c_l, \dots, a_N\rangle \quad [Z=3^N C_3] \\
 |G_{1,2}\rangle &\equiv \frac{1}{\sqrt{Z}} \sum_{(j \neq k \neq l)}^Z |a_1, a_2, \dots, g_j, \dots, c_k, \dots, c_l, \dots, a_N\rangle \quad [Z=3^N C_3]
 \end{aligned}$$

**Figure 12.** Collective states of figure 11 defined. For example,  $|A\rangle$  represents a state where all  $N$  atoms are in the single-atom state  $|a\rangle$ ,  $|G_1\rangle$  represents a symmetrized and normalized superposition of all states where only one of the  $N$  atoms is in the single-atom state  $|g\rangle$  and the rest are in the single-atom state  $|a\rangle$  and so on.

well as for measurements of Bell states [17], which in turn lie at the heart of many QIP protocols. However, as can be seen in figure 11, under such an excitation, the single- $\Lambda$  transition turns into a cascade of  $\Lambda$  transitions, involving collective states defined [14] in figure 12. As an aside, note that the number of states in the cascade depends on  $N$ , the number of atoms in the ensembles. For  $N = 1$ , the cascade disappears and is reduced to a simple  $\Lambda$  system.

In order to use ensembles as AQMs capable of performing useful functions in QIP, it is thus necessary to truncate this cascade. In [14, 15], we have shown how to do this, by making use of the so-called light shift blockade (LSB). Briefly, a light shift is the change in the energy of a state in the presence of a highly detuned laser field coupling it to another state. For off-resonant Raman transitions excited by unequal Rabi

frequencies, the difference in the shifts of the two metastable states is routinely taken into account in order to reach the two-photon resonance condition. For the Raman transitions shown in the cascades in figure 11, an imbalance in the Rabi frequencies can thus be used to prevent all but the primary (shown in shades) Raman transition from being two-photon resonant. The net effect, as summarized in figure 13, is that under the LSB, the ensemble acts as a single atom, so that the type of quantum storage, recall and processing illustrated in figure 6 through figure 9 can now be done with ensembles, loaded inside a cavity.

The advantage of using ensembles is that the coupling to a single photon is now enhanced by a factor of  $\sqrt{N}$ . However, since the Rabi frequencies in the cascade depend on  $N$ , the imbalance needed for truncating the cascade also depends on  $N$ . In particular, the blockade necessary for carrying out at least 100 operations is optimized for a value of about  $N = 1.5 \times 10^5$ , with an enhancement of about 400 in the vacuum Rabi frequency. It is well known that the vacuum Rabi frequency scales linearly with the length of a confocal cavity. Thus, a cavity about 2 cm long will have the same coupling strength as that of a 50  $\mu\text{m}$  long cavity typically used in a single-atom cavity QED experiment. For a given mirror reflectivity, the cavity storage time also increases with length. Therefore, the mirrors used in this cavity do not have to be as highly reflective as those used for the 50  $\mu\text{m}$  long cavity. We have previously identified the proper set of Hyperfine levels and Zeeman sublevels necessary for quantum storage and processing using ensembles of  $^{87}\text{Rb}$  atoms [14].

A simple configuration used for linking two such memory elements is illustrated in figure 14. Briefly, the quantum state encoded in the end ensemble of the quantum memory array on the left is read out, using the approach shown in figure 7. The resulting photonic qubit is then stored in the edge ensemble of the quantum memory array on the right. Of course, variations of this geometry can be used to store quantum information from a photonic qubit arriving from other

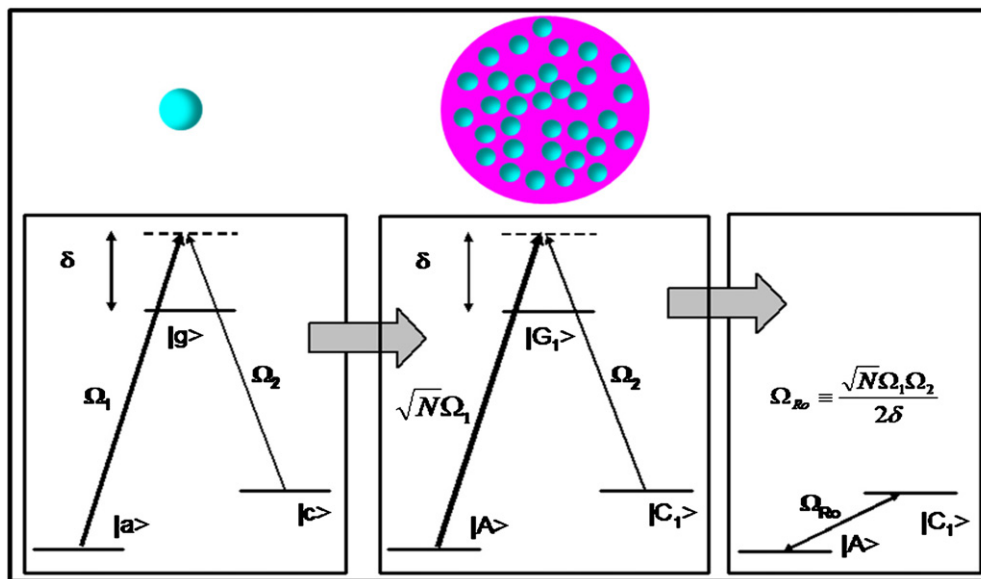


**Figure 13.** Summary of the LSB process, rendering an ensemble equivalent to a single atom.

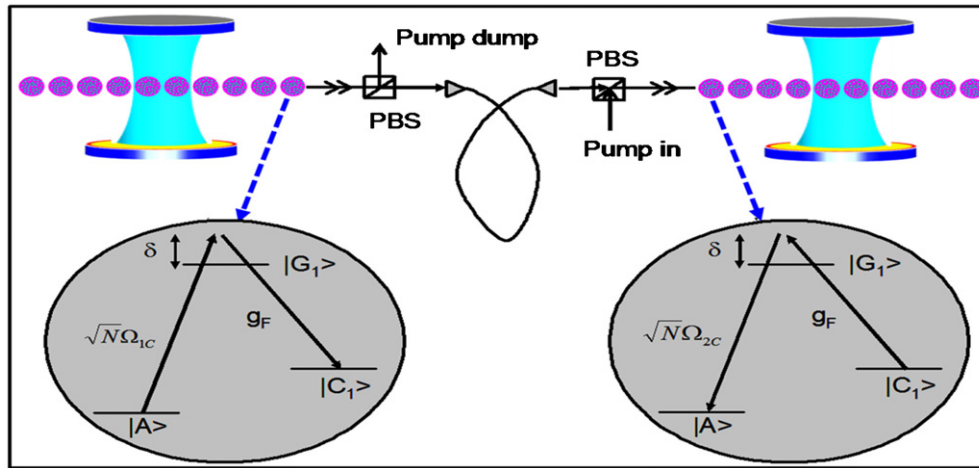


Figure 14. Illustration of quantum information retrieval and transfer.

sources. Furthermore, the photonic qubit restored from one ensemble can be converted to another frequency, and loaded into another quantum memory, as described in section 2.

#### 4. NV-diamond quantum memory

Bulk diamond and nanostructures of diamond containing an individually addressable nitrogen-vacancy colour centres (NVCC) have emerged as a very promising candidate medium for many of the tools needed for QIP, as evidenced by a large body of work [7, 19–25]. A single NVCC in a nanostructure is nearly an ideal quantum system. Under cryogenic conditions (at 10 K, for example), it should be possible to reach a quantum memory lifetime far exceeding 1 s using the electron spin, due to the fact that the electron spin population lifetime exceeds 100 s at cryogenic temperature [26], or a much longer lifetime by transferring the qubit into the nuclear spin [27]. Using a cryogenically cooled and spatially distinct colour centre, addressed by a confocal lens system, it is possible to realize a quantum memory and a source of entangled photons. Using a pair of such systems, it would then be feasible to realize important QIP functionalities, including storage and retrieval of quantum information and Bell state measurement, as key steps for quantum teleportation and quantum repeating.

To understand how NV diamond can become entangled with photons, it is first necessary to determine the energy level structure and selection rules for optical transitions. Solid-state systems are considerably more complex than free atoms. In particular, the spin–orbit coupling in free atoms which allows optical transitions to induce electron spin flips is usually quenched for colour centres in solids. Thus, the Raman schemes that were so central to the photon entanglement and storage schemes outlined earlier were predicted to be strictly forbidden. As a result of these predictions, progress towards spin-photon entanglement in NVCC and other solid-state systems was delayed by many years. However, recent developments showed that these negative predictions were too simplistic, and in fact spin-photon quantum entanglement was recently demonstrated for NV diamond.<sup>7</sup>

NV diamond consists of a carbon vacancy in the diamond lattice with one of the neighbouring carbon atoms substituted

by a nitrogen atom, as illustrated in figure 15(a). This vacancy can be thought of as a carbon atom with zero nuclear charge. The outer s and p orbitals of the carbon atoms in diamond satisfy the octet rule, and so the vacancy will also be assumed to prefer a full shell of eight electrons distributed among one s and three p orbitals. However, unlike a free atom, the p orbitals are not all degenerate. In particular, the NV centre has a symmetry of C3v, which means that there is a z-axis distortion. As a result, the s and pz levels are split out from the px and py orbitals. This is illustrated in figure 15(b), where the px and py orbitals are replaced by p+ and p– which have orbital angular momentum projections of +1 and –1 along the z-axis, respectively. Of course in the presence of non-axial strain or electric fields, the C3v symmetry is lowered and the px and py orbitals are no longer degenerate, as illustrated in figure 15(b).

The negatively charged NV-complex is the one of interest and has six electrons: four from the dangling bonds of the neighbouring atoms, one extra electron on the nitrogen, plus the electron needed to give the negative charge. Assuming that Hund’s rule for adding electrons to free atoms applies, the ground state will be a spin-1 triplet, as illustrated by the small arrows in the energy level diagram of figure 15(c). Since the shell is mostly full, it is more convenient to work with holes than electrons and these are shown by the large arrows in the level diagrams of figures 15(b) and (c).

Thus, the NV diamond ground state has equal contributions from p– and p+ orbitals which gives it a net orbital angular momentum projection of zero,  $m_L = 0$ . The electron spin triplet on the other hand has three possible projections,  $m_S = 0, -1, +1$ . Due to a weak spin–orbit interaction with the excited state, these levels split into a state with A-symmetry,  $|0\rangle$  and a degenerate pair of E-states  $|−1\rangle$  and  $|+1\rangle$  as illustrated in figure 15(d). This splitting is approximately 2.88 GHz. Of course, if an axial magnetic field is applied, the  $m_S = \pm 1$  states can also split (not shown).

In contrast, the excited state has a contribution from either p+ or p– but not both, and thus there are two orbital excited states, where the p+ triplet state for holes is shown in figure 15(c). Note that a singlet state is also possible but details

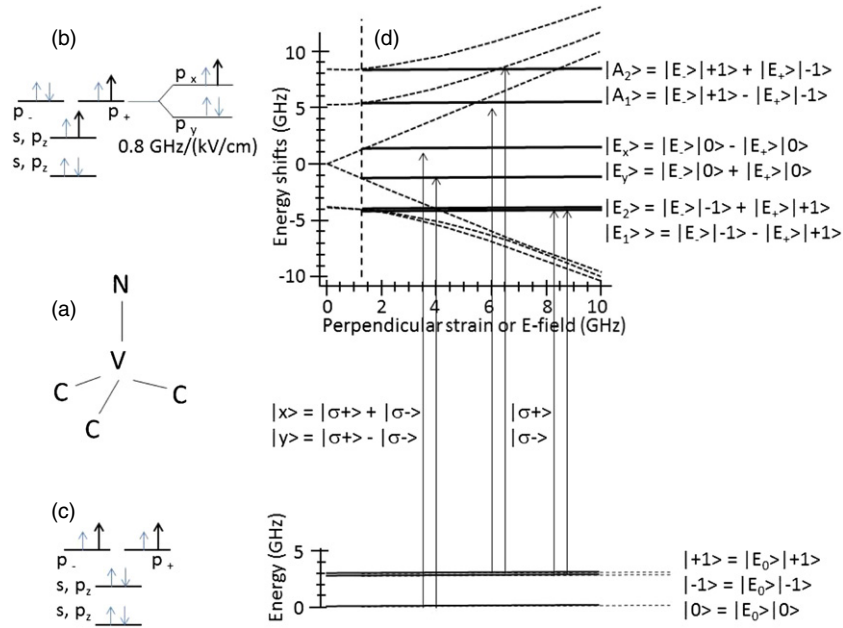


**Figure 15.** (a) The nitrogen-vacancy (NV) centre. (b) The excited-state energy levels showing the effects of strain. (c) The ground-state triplet. (d) The excited- and ground-state assignments are as labelled. The shifts of the energy levels with strain or electric field are shown as the dotted lines. At the strain shown by the vertical dashed line, the energy levels are extended in the horizontal direction to show the allowed optical transitions.

of this are not yet fully known and there are no allowed optical transitions to the singlet from the triplet ground state, since optically induced electron spin flips are forbidden. When the electron spin is included, there are a total of six excited states. The first two correspond to opposing orbital and spin quantum numbers  $m_L = +1, m_S = -1$  and  $m_L = -1, m_S = +1$ . Mutual spin flips between these levels are fully allowed and hence there is a strong interaction which leads to well-split superposition states with symmetries  $A_1$  and  $A_2$  as shown in figure 15(d). The next two states are the  $m_S = 0$  states. Mutual spin flips between these would correspond to  $\Delta m = 2$  and hence are forbidden. Nonetheless, even the slightest perturbation lifts the degeneracy of these states converting them into  $E_x$  and  $E_y$  as shown in figure 15(d). Finally, there are the states with total angular momentum quantum numbers of 2,  $m_L = +1, m_S = +1$  and  $m_L = -1, m_S = -1$ . Again spin flips are forbidden as these would require  $\Delta m = 4$ . Due to the relative insensitivity of electron spin to strain, these levels are not strongly split by strain. Although for large strains, the interaction with the  $E_y$  state can cause mixing as shown in figure 15(d). Note that the ground state levels are also insensitive to strain.

From the requirement that electron spin is preserved on optical excitation, the allowed optical transitions can be easily determined and are shown in figure 15(d) and in more detail in figure 16. Note that these transitions include fully allowed electron spin-flip Raman transitions, for example,  $|-1\rangle \rightarrow |A_2\rangle \rightarrow |+1\rangle$  even though all the optical spin-flip transitions are forbidden.

Using the transition manifold of figure 16, it is easy to show how to generate photons that are entangled with electron spin. For example, starting from the  $|A_2\rangle$  excited state, it is seen that an NV decaying to the  $|-1\rangle$  electron spin ground state will

emit a  $\sigma+$  photon, whereas decay to the  $|+1\rangle$  electron spin state will result in a  $\sigma-$  photon.<sup>7</sup> If this emitted photon is converted into the telecom band and then into a wavelength resonant with rubidium, it can be captured by the rubidium atom and in so doing produce entanglement between the NV spin and a distant Rb spin.

The inverse process of capturing an entangled photon emitted by a Rb atom and converting it into an entanglement between the NV and Rb is more complicated. Actually the first part is very simple, as shown in figure 16, since an NV starting from the spin  $|0\rangle$  ground state can absorb either an  $|x\rangle$  or a  $|y\rangle$  polarized photon to selectively populate states  $|E_y\rangle$  or  $|E_x\rangle$  as shown, in analogy to the Rb memory. However, to verify that absorption has occurred, the excited-state populations must be shelved to other long-lived states so that a cycling transition with either  $x$  or  $y$  polarization can verify whether or not a photon was absorbed, in analogy to the Rb case. How this can be accomplished is not immediately obvious from figure 16 since there are no optical transitions from  $|E_x\rangle$  or  $|E_y\rangle$  to a ground state other than  $|0\rangle$ , and hence there is no optical Raman transition that can be used to adiabatically transfer the population to any other states.

To overcome this problem, we introduce a microwave transition in the excited state. The relevant allowed transitions are as labelled in figure 17(a). This excitation scheme is known as the double dark technique [28]. It is not difficult to drive the ground- and excited-state microwave transitions in NV diamond at Rabi frequencies of the order of 1 GHz or larger which is much faster than the tens of MHz inhomogeneous width of the excited states. Thus, well-resolved Rabi splitting can be produced in the excited-state spin sublevels as illustrated in figure 17(b) for realistic parameters. As seen in figure 17(b), high-contrast Raman dark resonances are easily

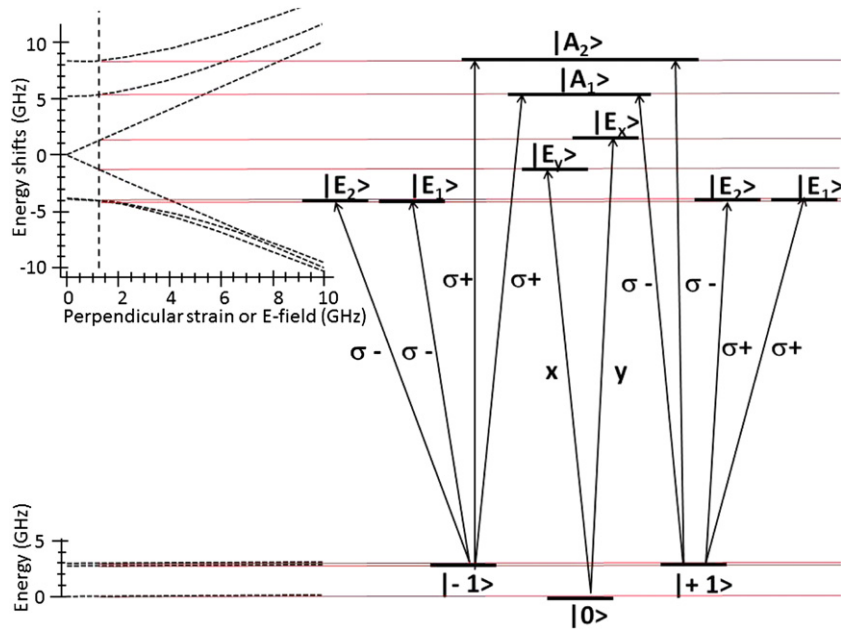


**Figure 16.** Details of the optical selection rules for the NV diamond transitions from the ground to excited triplet manifolds. As can be seen, electron-spin-flip Raman transitions are allowed even though the optical transition cannot flip electron spin.

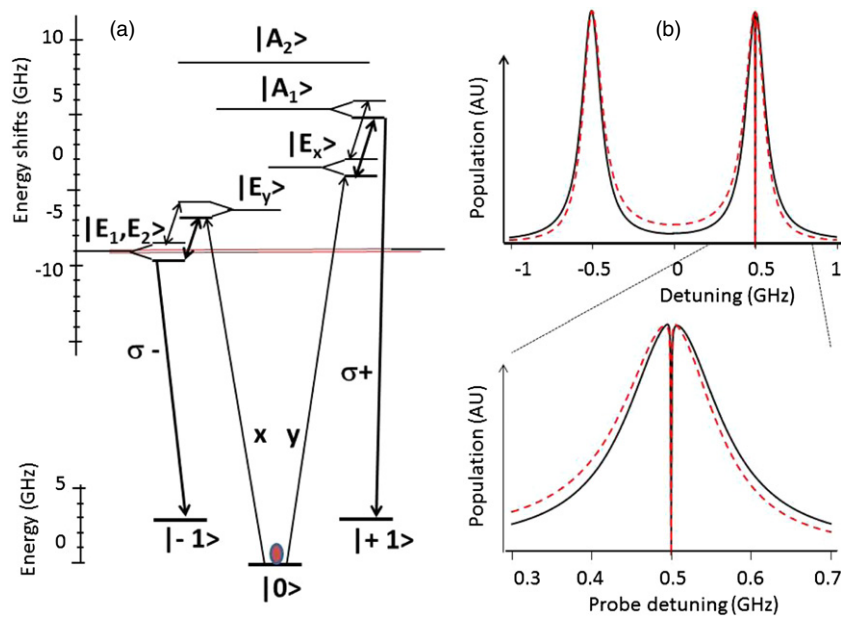


**Figure 17.** (a) Excitation scheme to transfer  $x, y$  polarization entanglement of an input (probe) photon into NV electron spin entanglement. As shown, the  $x$ -polarization is mapped onto the  $|-1\rangle$  spin state and the  $y$ -polarization is mapped onto the  $|+1\rangle$  spin state. (b) A representative plot of excited-state population versus detuning of input (probe) frequency showing efficient excitation of a Raman dark state. For these plots, the excitation scheme involving  $|E_x\rangle$  (solid curve) and  $|A_1\rangle$  (dashed curve) excited states is used. The microwave field is resonant with the  $|E_x\rangle$  to  $|A_1\rangle$  transition and has a Rabi frequency of 1 GHz. The probe and  $\sigma+$  Rabi frequencies are 10 MHz, where the  $\sigma+$  de-excitation field is detuned by half the microwave Rabi frequency, or 0.5 GHz, from the excited  $|A_1\rangle$  state. The excited-state linewidth is 100 MHz, and the ground-state linewidth is 1 kHz.

excited. Here it is worth emphasizing that the optical fields are not resonant with transition from the ground to excited state since then there would be no dark state. Instead the optical fields are detuned by one-half of the microwave Rabi frequency as shown in figure 17(a). Using this excitation scheme, the polarization and/or frequency entanglement present on an incoming photon can be stored in the NV spin states, just as was the case in the Rb memory. To verify that a photon

was captured, the optical transitions, labelled  $y$  in figure 17(a), starting from the  $m_S = 0$  ground can be driven. Since this is a cycling transition, many photons will be generated if the  $m_S = 0$  state is still populated. No detected photons means that the electron is in either of the  $m_S = +/- 1$  states. In this way, the successful storage of the input photon can be verified without disturbing its quantum state, in analogy with the technique used in Rb. Here it is worth noting that this double-dark excitation

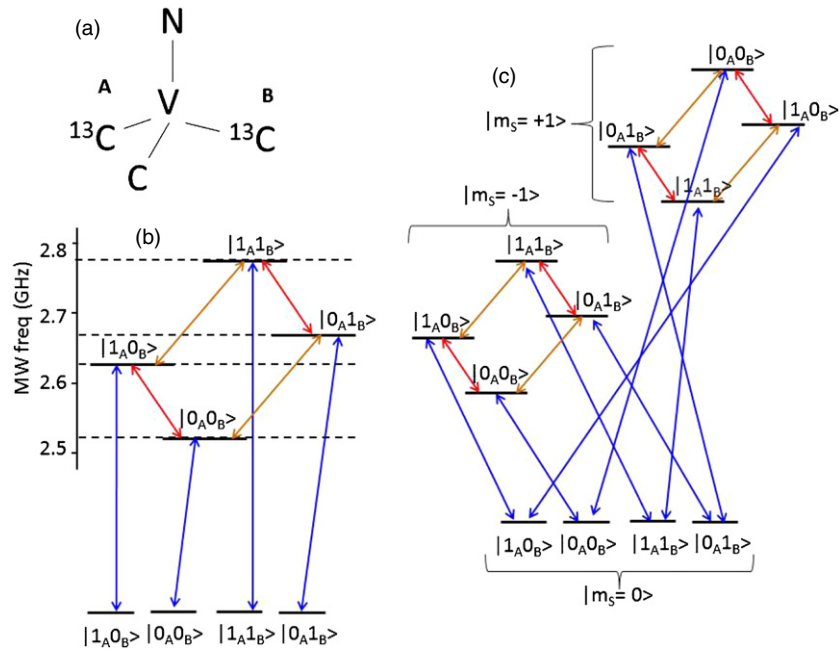


**Figure 18.** (a) NV with two adjacent  $^{13}\text{C}$  nuclei labelled A and B. (b) Partial energy level scheme and allowed transitions from the  $m_S = 0$  electron spin state to the  $m_S = -1$  state in a weak axial magnetic field. The nuclear spin state  $|0\rangle$  corresponds to spin up and  $|1\rangle$  to spin down. (c) The complete system including  $m_S = -1, 0, +1$ .

scheme is very general and can be used to produce efficient spin-flip Raman dark resonances in almost any system, even though no optical spin-flip transitions exist.

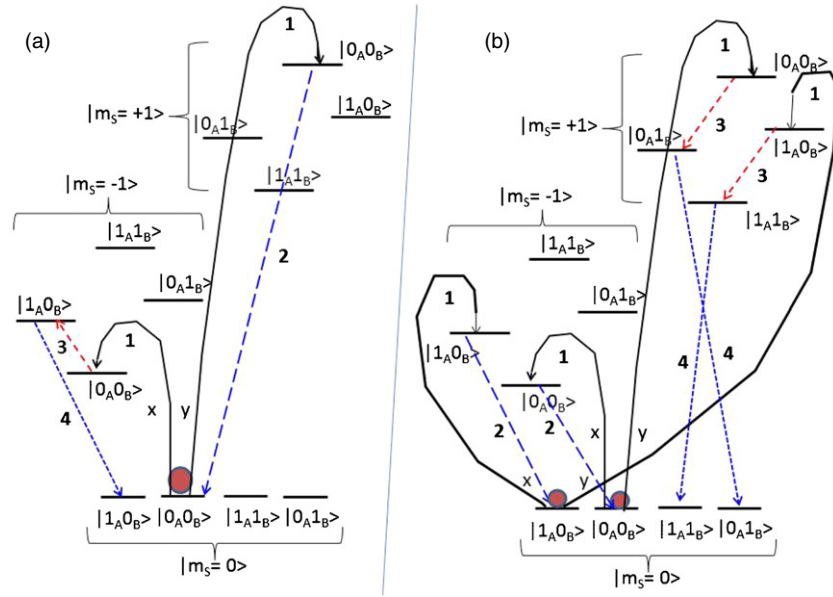
Once the quantum information has been deposited into a superposition of electron spin  $|+1\rangle$  and  $|-1\rangle$  states, it can be transferred into nuclear spin states where it can be stored for seconds to minutes or longer at low temperature. To perform quantum operations on the stored photons, like Bell state measurements, there are a variety of options. First, a pair of NVs with entangled electron spin can be used. Scalable quantum logic has already been demonstrated with such a pair coupled by magnetic dipole-dipole interactions at room temperature. Second, the optical dipole-dipole interaction between nearby NVs can be used to create an entangled pair for quantum logic. Third, cavity-mediated optical coupling can be used, or possibly microwave coupling using superconducting cavities. Fourth, for simple Bell state measurements involving two qubits as in quantum teleportation, a single NV with a pair of near-neighbour  $^{13}\text{C}$  nuclei can be used. In fact, efficient Bell state excitation was already demonstrated with this system at room temperature [24].

Figure 18 shows one possible scheme for capturing the quantum information from two photons and storing them on adjacent  $^{13}\text{C}$  spins of a single NV. Figure 18(a) shows two  $^{13}\text{C}$  nuclear spins labelled A and B in a single NV. Figure 18(b) shows how the  $m_S = 0$  to  $m_S = -1$  electron spin transition is split by the hyperfine interaction with the two adjacent  $^{13}\text{C}$  nuclei. As seen, each of the four nuclear spin combinations can be independently and conditionally driven between electron spin 0 and  $-1$  states with resonant microwave (MW) fields. In addition, radio frequency (RF) fields can drive spin flips of one nuclear spin at a time. Note that the two-spin states  $|1_A 0_B\rangle$  and  $|0_A 1_B\rangle$  are degenerate and can undergo mutual

spin flip-flops. This leads to a strong interaction that gives superposition eigen-states with a relatively large splitting as shown. However, for the purpose of quantum storage, it does not matter whether these states are pure two-spin states or not as long as the transitions shown are allowed. Therefore, for simplicity the pure-state notation is used.

To store the photon quantum state in the nuclear spins, both  $m_S = -1$  and  $m_S = +1$  transition manifolds are needed and these are shown in figure 18(c). Storage of the quantum state of the first photon begins by initializing the nuclear spins into a single-composite state as shown in figure 19(a). This can be done by simultaneously driving the  $m_S = +/-1$  optical transitions, plus the  $m_S = 0 \rightarrow +/-1$  ground-state microwave transitions for all nuclear spin states except the  $|0_A 0_B\rangle$  state (not shown). Electron and nuclear flip-flops in the optical excited state eventually put all the nuclear spins into the  $|0_A 0_B\rangle$   $|m_S = 0\rangle$  ground state because this state is not excited by either optical or microwave fields.

Once initialized, the quantum state encoded in the polarization of the first photon is mapped onto the NV electron spin using the technique of figure 17, and illustrated schematically by step ‘1’ in figure 19(a). This mapping of quantum information from the photon to the electron spin preserves nuclear spin states. Next the quantum information stored on the electron spin must be transferred to one of the nuclear spins. This is done using the remaining steps in figure 19(a). In particular, step ‘2’ shelves the  $|0_A 0_B\rangle$  state, originally in the  $m_S = +1$  manifold, into the  $m_S = 0$  manifold with a microwave  $\pi$  pulse, as shown by the transitions labelled ‘2’. Next the first nuclear spin is flipped conditioned on the electron being in the  $m_S = -1$  manifold by using a RF  $\pi$  pulse as shown by the transition labelled ‘3’. Thus, the first nuclear spin is flipped only if the input photon was x-polarized.



**Figure 19.** (a) NV with two adjacent  $^{13}\text{C}$  nuclei labelled A and B. (b) Partial energy level scheme and allowed transitions from the  $m_S = 0$  electron spin state to the  $m_S = -1$  state in a weak axial magnetic field. The nuclear spin state  $|0\rangle$  corresponds to spin up and  $|1\rangle$  to spin down. (c) The complete system including  $m_S = -1, 0, +1$ .

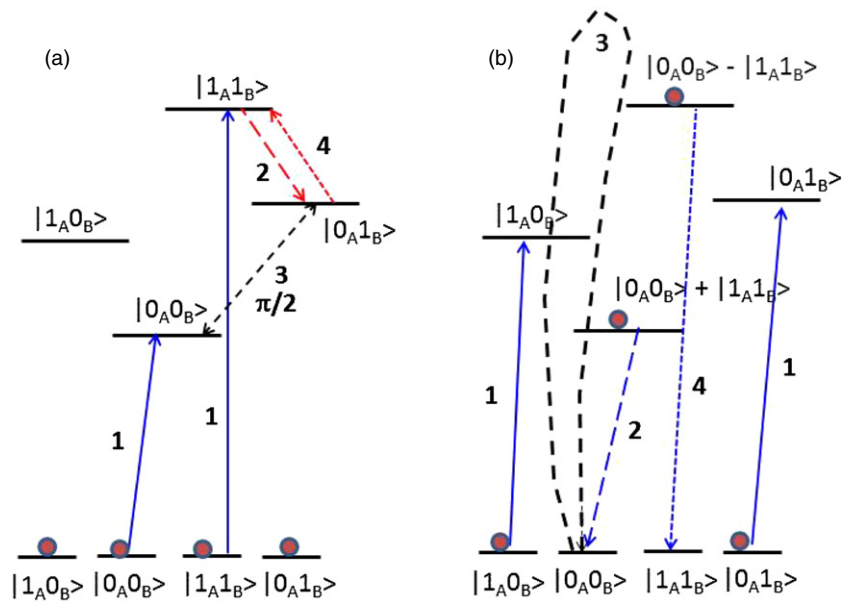


**Figure 20.** (a) Bell state readout starts by moving the desired composite states into the  $m_S = -1$  manifold. To rotate these into the Bell basis, a  $\pi/2$  pulse, labelled 3, is needed. Due to selection rules, this is preceded and followed by  $\pi$  pulses labelled 2 and 4. (b) Once rotated into the Bell basis, the states can be read out one at a time using the optical cycling transition on the  $m_S = 0$  manifold. This is illustrated for  $\Phi+$ .

Finally, this flipped nuclear spin is also shelved into the  $m_S = 0$  manifold, as shown by the transitions labelled ‘4’, to complete the electron to nuclear quantum state mapping, and to preparation for the second photon.

The second photon is then captured and its quantum information stored in its polarization state is mapped onto the electron spin  $m_S = +/-1$  states, as for the first photon, as shown by step 1 in figure 19(b). Again this is done without changing nuclear spins, on which the quantum state of the first photon is stored. Step 2 protects the information in the  $m_S = -1$  manifold by transferring it to the  $m_S = 0$  manifold

with dual  $\pi$  pulses as shown. Then step 3 flips the second nuclear spin B conditioned on the electron being in the  $m_S = +1$  manifold without disturbing the coherence on nuclear spin A. Finally, these flipped nuclear spins are transferred to the  $m_S = 0$  manifold in step 4 in preparation for Bell state measurements.

The Bell state measurement sequence is illustrated in figure 20. In figure 20(a), step 1 selectively transfers the  $|00\rangle$  and  $|11\rangle$  states onto the  $m_S = -1$  manifold with dual  $\pi$  pulses. To convert these into Bell states, a  $\pi/2$  pulse is needed on the transition between them. However, this transition is forbidden

by selection rules and so the  $\pi$  pulses in steps 2 and 4 are needed before and after the  $\pi/2$  pulse (step 3). To read out the Bell state probabilities, the remaining nuclear spin states are first transferred out of the  $m_S = 0$  manifold (step 1 in figure 20(b)) as this has the cycling transition needed for readout. In step 2, the desired Bell state is selectively transferred to the  $m_S = 0$  manifold by a MW  $\pi$  pulse as shown. Step 3 is the optical readout which determines if  $\Phi_+$  was occupied. Step 4 shows the transfer of  $\Phi_-$  for readout in the event  $\Phi_+$  was found to be unoccupied. The remaining steps are not shown but follow a similar procedure.

In this section, the basic scheme for transferring the quantum information of two incoming photons, for example, from a Rb atomic memory, onto the NV electron spin has been outlined. The inverse process of generating photons whose polarization state is entangled with the NV electron spin was previously demonstrated experimentally [7]. Furthermore, the technique for transferring the electron-spin quantum states onto  $^{13}\text{C}$  nuclear spins for long-term storage has also been outlined. Finally, the use of two  $^{13}\text{C}$  nuclei on a single NV for making Bell state measurements was outlined. Thus, NV diamond has all the key elements needed for interfacing to trapped Rb atoms in a telecom-based quantum internet.

## 5. Summary and outlook

We have described techniques for creating quantum links at the telecom band between different types of quantum memories, using PPLN waveguides. The specific QMs we consider are based on ensembles of Rb atoms and nitrogen vacancy colour centres, each configured for processing capabilities. Memories based on spectral hole burning media could also be connected in this manner [29]. Links of this type could serve as the key interface needed for building a quantum internet.

## Acknowledgments

This work was supported in part by AFOSR grant FA9550-09-01-0652 and DARPA QuEST.

## Q4 References

- [1] Duan L M, Lukin M D, Cirac J I and Zoller P 2001 *Nature* **414** 413
- [2] Sangour N *et al* 2007 *Phys. Rev. A* **76** 050301
- [3] Molina-Terriza G, Torres J P and Torner L 2002 *Phys. Rev. Lett.* **88** 013601
- [4] Mair A, Vaziri A, Weihs G and Zeilinger A 2001 *Nature* **412** 313
- [5] Broadbent C J, Camacho R M, Xin R and Howell J C 2008 Preservation of energy-time entanglement in a slow light medium *Phys. Rev. Lett.* **100** 133602
- [6] Huang J and Kumar P 1992 Observation of quantum frequency conversion *Phys. Rev. Lett.* **68** 2153–6
- [7] Togan E *et al* 2010 Quantum entanglement between an optical photon and a solid-state spin qubit *Nature* **466** 730
- [8] Zhu X *et al* 2011 Coherent coupling of a superconducting flux qubit to an electron spin ensemble in diamond *Nature* **478** 221
- [9] Ladd T D, Jelezko F, Laflamme R, Nakamura Y, Monroe C and O'Brien J L 2010 Quantum computers *Nature* **464** 45
- [10] Buluta I, Ashhab S and Nori F 2011 Natural and artificial atoms for quantum computation *Rep. Prog. Phys.* **74** 104401
- [11] Kumar P 1990 Quantum frequency conversion *Opt. Lett.* **15** 1476–8
- [12] Boyd R W 2003 *Nonlinear Optics* 2nd edn (Edinburgh: Academic)
- [13] Huang J and Kumar P 1992 Observation of quantum frequency conversion *Phys. Rev. Lett.* **68** 2153–6
- [14] Shahriar M S, Pati G S and Salit K 2007 Quantum communication and computing with atomic ensembles using light-shift imbalance induced blockade *Phys. Rev. A* **75** 022323
- [15] Shahriar M S, Pradhan P, Pati G S and Salit K 2007 Light-shift imbalance induced blockade of collective excitations beyond the lowest order *Opt. Commun.* **278** 94–8
- [16] Pellizzari T, Gardiner S A, Cirac J I and Zoller P 1995 Decoherence, continuous observation, and quantum computing: a cavity QED model *Phys. Rev. Lett.* **75** 3788
- [17] Lloyd S, Shahriar M S, Shapiro J H and Hemmer P R 2001 Long distance, unconditional teleportation of atomic states via complete bell state measurements *Phys. Rev. Lett.* **87** 167903
- [18] Deutsch D, Ekert A, Jozsa R, Macchiavello C, Poescu S and Sanpera A 1996 Quantum privacy amplification and the security of quantum cryptography over noisy channels *Phys. Rev. Lett.* **77** 2818–21
- [19] Shahriar M S, Hemmer P R, Lloyd S, Bhatia P S and Craig A E 2002 Solid-state quantum computing using spectral holes *Phys. Rev. A* **66** 032301
- [20] Hemmer P R, Turukhin A V, Shahriar M S and Musser J A 2001 Raman excited spin coherence in NV-diamond *Opt. Lett.* **26** 6
- [21] González G and Leuenberger M N 2009 Optical  $\Lambda$  transitions and quantum computing in the  $^{15}\text{N-V}^-$  center in diamond *Phys. Rev. B* **80** 201201
- [22] Gaebel T *et al* 2006 Room-temperature coherent coupling of single spins in diamond *Nature Phys.* **2** 408–13
- [23] Childress L, Gurudev Dutt M V, Taylor J M, Zibrov A S, Jelezko F, Wrachtrup J, Hemmer P R and Lukin M D 2006 Coherent dynamics of coupled electron and nuclear spin qubits in diamond *Science* **314** 281–5
- [24] Neumann P, Mizuochi N, Rempp F, Hemmer P, Watanabe H, Yamasaki S, Jacques V, Gaebel T, Jelezko F and Wrachtrup J 2008 Multiparticle entanglement among single spins in diamond *Science* **320** 1326–9
- [25] Jiang L *et al* 2009 Repetitive readout of a single electronic spin via quantum logic with nuclear spin ancillae *Science* **326** 267–72
- [26] Harrison J, Sellars M J and Manson N B 2006 Measurement of the optically induced spin polarisation of N-V centres in diamond *Diamond Relat. Mater.* **15** 586–8
- [27] Balasubramanian G *et al* 2009 Ultralong spin coherence time in isotopically engineered diamond *Nature Mater.* **8** 383–7
- [28] Yelin S F, Sautenkov V A, Kash M M, Welch G R and Lukin M D 2003 Nonlinear optics via double dark resonances *Phys. Rev. A* **68** 063801
- [29] Clausen C, Usmani I, Bussi eres F, Sangouard N, Afzelius M, Riedmatten H and Gisin N 2011 Quantum storage of photonic entanglement in a crystal *Nature* **469** 508–11

## QUERIES

### Page 1

#### Q1

Author: Please be aware that the colour figures in this article will only appear in colour in the Web version. If you require colour in the printed journal and have not previously arranged it, please contact the Production Editor now. If you choose not to pay for colour printing, please amend reference to colour in the text.

### Page 5

#### Q2

Author: Please check whether the edit made in the caption to figure 6 retains your intended sense.

### Page 7

#### Q3

Author: Figure 10 is not cited in the text. Please check.

### Page 14

#### Q4

Author: Please check the details for any journal references that do not have a blue link as they may contain some incorrect information. Pale purple links are used for references to arXiv e-prints.

#### Q5

Author: Please check whether the author names are okay as set in reference [10].